Frontiers of Information Technology & Electronic Engineering
www.jzus.zju.edu.cn; engineering.cae.cn; www.springerlink.com
ISSN 2095-9184 (print); ISSN 2095-9230 (online)
E-mail: jzus@zju.edu.cn

Design of omnidirectional Rydberg atomic sensors loaded with electric field enhancement structure using characteristic mode analysis*

Zhenke DING, Yi LIU†‡, Bo WU, Kai YANG, Ruibing RAN, Yi LIN, Yunqi FU

College of Electronic Science and Technology, National University of Defense Technology, Changsha 410073, China

†E-mail: yi_liu@nudt.edu.cn

Received Aug. 10, 2024; Revision accepted Mar. 4, 2025; Crosschecked July 10, 2025

Abstract: The integration of electric field enhancement structures (EFESs) with Rydberg atomic sensors (RASs) has garnered considerable interest due to their potential to enhance detection sensitivity in quantum measurement systems. Despite this, there is a dearth of research on the directional response of EFES, and the analysis of the three-dimensional (3D) patterns of RAS remains a formidable challenge. RASs are employed in non-destructive measurement techniques, and are responsive to electric fields, primarily serving as reception devices. However, analyzing their reception patterns is a complex task that requires a sophisticated approach. To address this, we adopt characteristic mode (CM) analysis to illustrate the omnidirectional performance of RAS. According to the CM theory, the reception pattern can be calculated by a series of modal currents and their corresponding coefficients. The analytical representation of these coefficients negates the need for time-consuming full-wave (FW) numerical simulations, which are typically required to generate EFES patterns due to the necessity of scanning numerous angle parameters. This approach significantly reduces the complexity of solving EFES patterns, and provides insightful guidance for the design process. To validate the efficacy of our proposed method, we construct three prototypes. The results indicate that the final model resonates at 1.96 GHz, achieving an electric field gain of 25 dB and an out-of-roundness of 2.4 dB. These findings underscore the effectiveness of our method in analyzing EFES patterns, highlighting its potential for future applications in the field.

Key words: Rydberg atomic sensor; Characteristic mode; Electric field enhancement structure
https://doi.org/10.1631/FITEE.2400700 **CLC number:** TM13; TP212

1 Introduction

Quantum precision measurement technology based on quantum theory provides a novel pathway for measuring physical parameters. This technology has the characteristic of self-calibration, and enables the absolute measurement of physical quantities (Sedlacek et al., 2012). Over the past decade, researchers have been exploring its application in microwave electric field measurement, with the most typical being Rydberg atom-based electric field measurement technology (Sedlacek et al., 2012, 2013; Holloway et al., 2014; Yang et al., 2022; Zhang FS et al., 2023). The theoretical detection sensitivity of microwave electric field measurement based on quantum theory is higher than that of traditional electronic microwave measurement systems (Fan et al., 2015). However, there is still a significant gap between the measurement values of detection sensitivity and the theoretical values (Dixon et al., 2023; Mao et al., 2023; Zhang FS et al., 2023; Sandidge et al., 2024; Yuan et al., 2024).

Rydberg atom-based microwave electric field

‡ Corresponding author
* Project supported by the National Natural Science Foundation of China (Nos. 61901495, 62401586, and U24B2009) and the Hunan Provincial Natural Science Foundation (No. 2022JJ40556)
ORCID: Yi LIU, https://orcid.org/0000-0002-2558-444X

measurement principles provide avenues for improving detection sensitivity, with two main approaches: quantum optical methods (Bussey et al., 2021; Liu et al., 2022; Yang et al., 2023b) and microwave methods (Holloway et al., 2022; Wu et al., 2022, 2023; Yang et al., 2023c). Recent advancements in microwave methods, including heterodyne detection (Simons et al., 2021; Yao et al., 2022), modulation signals (Meyer et al., 2018; Holloway et al., 2019; Jiao et al., 2019; Song et al., 2019; Yang et al., 2023a), multi-channel detection (Robinson et al., 2021; Hu et al., 2023), and the electric field enhancement structures (EFESs) loaded method (Holloway et al., 2022; Yang et al., 2023c; Sandidge et al., 2024), have shown promise in improving the detection sensitivity of Rydberg atom-based systems. EFESs act as a special boundary condition added to the Rydberg atomic sensors (RASs), thereby altering the electric field response of the sensors to incident waves. EFES can enhance the electric field in a specific area, thus improving detection sensitivity. It should be noted that the difference between the RASs and antennas is that RASs respond to the electric field in space rather than capturing the electromagnetic power density. Therefore, RASs do not prioritize impedance matching when receiving microwave but concentrate on the degree of electric field enhancement.

One of the influencing factors of the directional response of RASs is the direction of the incident electric field. It is necessary for RAS to study directionality to meet the different application requirements. Consequently, the EFES pattern should be defined as the electric field amplitude gain (E-Gain) pattern. An omnidirectional pattern is commonly used for direction finding (Choi and Sarabandi, 2018; Ren, 2022). Researchers have found that the response of RASs to incident waves is approximately isotropic (Anderson et al., 2021; Mao et al., 2023; Yuan et al., 2024), meaning that RASs are similar to the dipole antennas with good omnidirectional performance. Currently, few scholars have studied EFES's response to incident waves from different directions. While the use of EFES enhances detection sensitivity, it could potentially impact the omnidirectional performance of the sensors. Balancing the E-Gain and the omnidirectional performance of the sensors is a challenge.

Furthermore, RASs cannot be used for radiation applications in the current research stage. This means that when studying the directional response of EFES, we cannot obtain its radiation pattern and reception pattern through port excitation based on the reciprocity theorem. The EFES pattern solution is similar to solving the scattering problem of a near field. RAS is an electric field probe close to EFES under microwave irradiation. The current analysis approach requires configuring angle parameters in full-wave (FW) simulation software to acquire reception patterns via parameter scanning. The measurement method follows the same approach. It costs too much calculation time to complete pattern design and optimization. However, there is no better way to obtain the reception pattern of EFES. Most of the current research explored the E-Gain for EFES only at a fixed incident angle (Anderson et al., 2018; Holloway et al., 2022; Yang et al., 2023c). Therefore, researching directionality analysis methods for EFES is of great significance in improving the sensitivity of Rydberg atom probes in microwave electric field measurement.

In a word, EFES is a special boundary condition for RASs. The directional response of EFES is consistent with that of the integration sensors. Typically, EFES is composed of metal and dielectric materials, generally similar to a split-ring resonator (SRR) (Holloway et al., 2022). The sensors can be simply considered as a glass bubble filled with air in electromagnetic wave propagation. In the field of antennas, by analyzing the modal currents on the metal surface through the characteristic mode (CM) theory (Harrington and Mautz, 1971), it is possible to control the radiation or scattering modes, and to calculate the classical circuit parameters (Chen and Wang, 2015; Huang et al., 2018; Grundmann and Manteuffel, 2021; Adams et al., 2022; Manteuffel et al., 2022; Zhang D et al., 2022; Dicandia and Genovesi, 2023; Shi et al., 2023). Meanwhile, in the CM theory, CMs are independent of external sources, and the EFES is a passive structure without feed-ports. The CM theory may be suitable for guiding EFES design. Only the external source contains the parameters related to the incident angle in the E-Gain patterns. Based on the CM theory, the EFES pattern can be expressed as the product of a set of modal electric fields and corresponding coefficients. The modal electric field depends on the external source and the corresponding coefficients can be calculated analytically, reducing the complexity of the solution.

Therefore, we believe that applying the CM theory to the design of EFES is a wise and feasible solution. We will analyze the patterns by examining the EFES modal currents based on the CM theory. It could provide a clear physical explanation and a better design method for EFES just like guiding antenna design.

2 Analysis of the mode pattern

2.1 Basic theory for Rydberg atom electric field measurement

Fig. 1a shows the two-photon Rydberg electromagnetically induced transparency (EIT) ladder scheme. There are two laser resources: one with a power of 14.6 mW at 509 nm and the other with 8.3 μW at 852 nm. The 852 nm laser is locked to one of the $6S_{1/2} \rightarrow 6P_{3/2}$ transitions with a Rabi frequency Ω_P. Similarly, the 509 nm laser is locked to the $6P_{3/2} \rightarrow 50S_{1/2}$ transitions with a Rabi frequency Ω_C. The EIT signal is then detected by a photodetector. When the radio-frequency (RF) resource is turned off, the EIT signal has only one peak, similar to the blue line in Fig. 1b. When the RF is turned on and the power is limited, the EIT signal will produce the alternating current (AC) Stark shift. The blue line will shift to the orange line (Cardman et al., 2020). The spectral shift Δf between the two peaks is related to the electric field magnitude $\|\boldsymbol{E}\|$ and can be expressed as (Cardman et al., 2020)

$$\Delta f = -\frac{1}{4}\alpha_0 \|\boldsymbol{E}\|^2, \tag{1}$$

where α_0 is the dynamic scalar polarizability. Fig. 1c shows the experimental setup overview. The sensor is the same as those in Mao et al. (2023) and Wu et al. (2024), as shown in Fig. 1c. An oscilloscope is used to measure the EIT signals received by a photodetector.

2.2 Current distribution for the enhanced electric field

According to the measurement theory of RASs (Sedlacek et al., 2012), it is expected that there is a strong electric field in the atomic cell center of RAS, and the polarization should be consistent with the polarization of the optical path, which is typically $+\boldsymbol{e}_z$. To avoid the distribution of the electric field

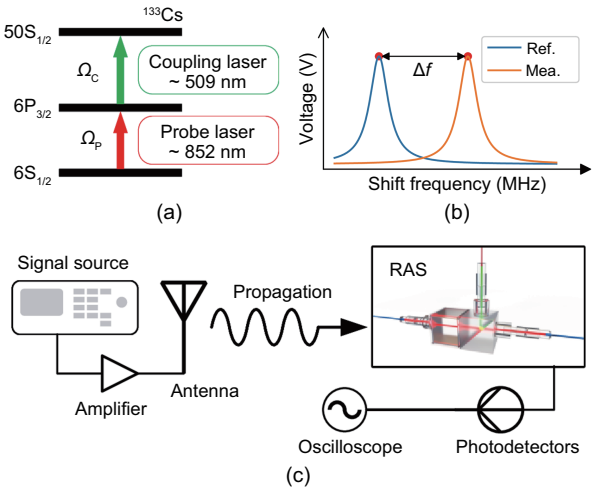

Fig. 1 Overview of the experimental energy diagram: (a) two-photon Rydberg EIT ladder scheme; (b) diagram of the AC-Stark frequency shift; (c) sketch of the atom experimental setup. References to color refer to the online version of this figure

with zero points like TE_{30}, the direction of the electric field in the cell should be the same. Therefore, it is recommended that adding the perfect electric conductor (PEC) condition on the cell of $z_{\max}$ and $z_{\min}$ enhances the electric field as shown in Fig. 2a. According to the current continuity equation (Harrington, 2001), it can be expressed as

$$\boldsymbol{J}_{\mathrm{d}} = \frac{\partial \boldsymbol{D}}{\partial t} = \varepsilon \frac{\partial \boldsymbol{E}}{\partial t}, \tag{2}$$

$$\nabla \left(\boldsymbol{J} + \frac{\partial \boldsymbol{D}}{\partial t} \right) = 0, \tag{3}$$

where $\boldsymbol{J}$, $\boldsymbol{J}_{\mathrm{d}}$, $\boldsymbol{D}$, $\boldsymbol{E}$, t, and ε represent conduction current, displacement current density, electrical flux density, electric field, time, and dielectric constant, respectively. EFES converts weak electromagnetic waves in space into a localized enhanced electric field, leading to the presence of enhanced displacement current $\boldsymbol{J}_{\mathrm{d}}$ in the region where the electric field is enhanced. Therefore, a metallic conductor is needed between the upper and lower plates to carry conduction current. It can also be regarded as the

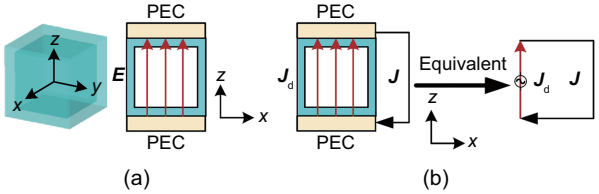

Fig. 2 View of the atomic cell and expected electric field (a) and the equivalent current model (b)

resonant current model of the SRR.

Therefore, a current model is proposed as shown in Fig. 2b. A conduction current can be achieved by connecting two metal nodes outside the PEC boundaries. When $\boldsymbol{J}$ as shown in Fig. 2b is constructed by only one conduction current, the most typical EFES model is named path 1 as shown in Fig. 3. The current distributions in Holloway et al. (2022) and Wu et al. (2023, 2024) are also consistent with that in path 1. Based on this current model and simple rotational symmetry, we can propose models with more conduction current paths as shown in Fig. 3. To understand the operating mechanism of the proposed structure, the intrinsic CMs supported by the structure are investigated using CM analysis.

2.3 Resonance CMs of EFES

When an RAS is loaded with EFES, the electric field at the center position of the atomic cell is an important parameter for analysis. The E-Gain is defined as the amplitude of the electric field at the center point of the atom cell under the excitation of a unit amplitude uniform plane wave.

To realize the proposed current model and study the corresponding pattern, the CM theory is introduced for analysis. According to the CM theory (Chen and Wang, 2015), the electric field $\boldsymbol{E}(\boldsymbol{r}_i)$ at any point $\boldsymbol{r}_i$ can be represented by a set of orthogonal CM electric fields $\boldsymbol{E}_m$ as

$$\boldsymbol{E}(\boldsymbol{r}_i)=\sum_m a_m\boldsymbol{E}_m(\boldsymbol{r}_i)=\sum_m\frac{<\boldsymbol{E}_{\rm inc},\boldsymbol{J}_m>}{1+{\rm j}\lambda_m}\boldsymbol{E}_m(\boldsymbol{r}_i), \tag{4}$$

$$a_m=\frac{<\boldsymbol{E}_{\rm inc},\boldsymbol{J}_m>}{1+{\rm j}\lambda_m}, \tag{5}$$

$${\rm MS}=\frac{1}{\|1+{\rm j}\lambda_m\|}, \tag{6}$$

where a_m, MS, $\boldsymbol{J}_m$, $\boldsymbol{E}_m(r_i)$, λ_m, and $\boldsymbol{E}_{\rm inc}$ represent the $m^{\rm th}$ modal weighting coefficient (MWC), modal significance, $m^{\rm th}$ modal current density, $m^{\rm th}$ modal electric field at point $\boldsymbol{r}_i$, $m^{\rm th}$ eigenvalue, and incident electric field, respectively. $<\cdot,\cdot>$ is the inner product. It should be noted that MS is an intrinsic property representing the coupling capability of each CM with external sources.

2.4 Pattern for EFES using CM theory

To study the directional response between incident electric field $\boldsymbol{E}_{\rm inc}$ and the EFES, a uniform plane wave is used as the incident wave. A unit uniform plane wave $\boldsymbol{E}_{\rm inc}$ propagating in any direction can be expressed as

$$\boldsymbol{E}_{\rm inc}=\boldsymbol{E}_{\rm amp}{\rm e}^{-{\rm j}\boldsymbol{k}\boldsymbol{r}}, \tag{7}$$

$$\begin{aligned}\boldsymbol{E}_{\rm amp}=&\,\boldsymbol{e}_x(\cos\theta\cos\varphi\cos\alpha-\sin\varphi\sin\alpha)\\&+\boldsymbol{e}_y(\cos\theta\sin\varphi\cos\alpha+\cos\varphi\sin\alpha)\\&-\boldsymbol{e}_z(\sin\theta\cos\alpha),\end{aligned} \tag{8}$$

$$\boldsymbol{k}=(\boldsymbol{e}_x\sin\theta\cos\varphi+\boldsymbol{e}_y\sin\theta\sin\varphi+\boldsymbol{e}_z\cos\theta)k, \tag{9}$$

$$\boldsymbol{r}=\boldsymbol{e}_x x+\boldsymbol{e}_y y+\boldsymbol{e}_z z, \tag{10}$$

where $\boldsymbol{E}_{\rm amp}$, $\boldsymbol{k}$, k, and $\boldsymbol{r}$ represent the electric field amplitude vector, wave vector, phase constant, and propagation vector, respectively. α represents the rotation angle of the electric field vector relative to the x-axis, and φ and θ represent the spherical angle coordinates of the incident plane wave. According to Eqs. (7)–(10), the unit uniform incident plane wave vector $\boldsymbol{E}_{\rm inc}$ can be expressed as

$$\boldsymbol{E}_{\rm inc}=\boldsymbol{E}(\alpha,\varphi,\theta,k). \tag{11}$$

The EFES pattern $G(\alpha,\varphi,\theta)$ is defined as

$$G(\alpha,\varphi,\theta)=\frac{\|\boldsymbol{E}_1(\boldsymbol{r}_i)\|}{\|\boldsymbol{E}_0(\boldsymbol{r}_i)\|}, \tag{12}$$

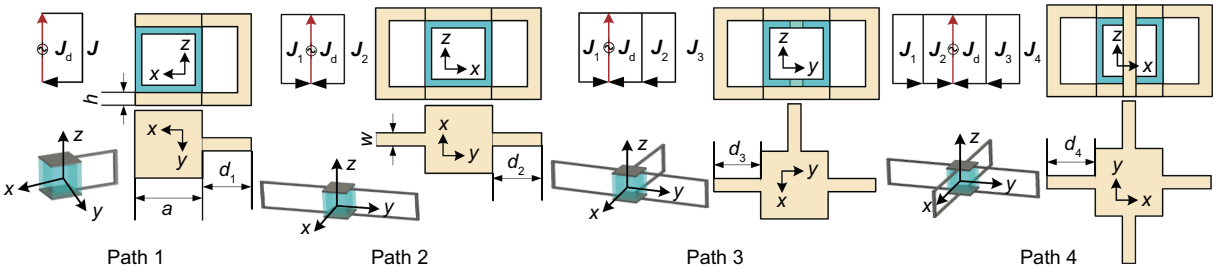

Fig. 3 The equivalent current model and corresponding physical structure. Four models are named paths 1, 2, 3, and 4. d_1=14 mm, d_2=27.4 mm, d_3=34.3 mm, d_4=38.8 mm, w=1 mm, h=0.5 mm, a=10 mm

where $\boldsymbol{E}_1(\boldsymbol{r}_i)$ and $\boldsymbol{E}_0(\boldsymbol{r}_i)$ represent the electric field in the atom cell with and without EFES, respectively. Substituting Eq. (7) into Eq. (4), the electric field at any point can be written as

$$\boldsymbol{E}(\boldsymbol{r}_i)=\sum_m \frac{<\boldsymbol{E}(\alpha,\varphi,\theta,k),\boldsymbol{J}_m>}{1+\mathrm{j}\lambda_m}\boldsymbol{E}_m(\boldsymbol{r}_i). \quad (13)$$

$\boldsymbol{J}_m$, λ_m, and $\boldsymbol{E}_m(\boldsymbol{r}_i)$ can be calculated by one CM analysis, and these parameters are related only to structure parameters. Substituting Eq. (13) into Eq. (12), the E-Gain $G(\alpha,\varphi,\theta)$ is expressed as

$$G(\alpha,\varphi,\theta)=\frac{\left\|\sum_m \frac{<\boldsymbol{E}(\alpha,\varphi,\theta,k),\boldsymbol{J}_m>}{1+\mathrm{j}\lambda_m}\boldsymbol{E}_m(\boldsymbol{r}_i)\right\|}{\|\boldsymbol{E}_0(\boldsymbol{r}_i)\|}. \quad (14)$$

Eq. (14) implies that the pattern of EFES can be calculated through a single CM analysis. Traditional analysis methods typically require multiple times FW simulations by scanning parameters, resulting in a computation of the three-dimensional (3D) directional pattern for $n\times m\times l$ sampling points, where n, m, and l represent the numbers of sampled points for α, φ, and θ, respectively. By contrast, the proposed method reduces the computation to a single CM analysis, significantly reducing the simulation time compared with traditional methods. Combined with the CM theory, it provides a convenient method of analysis from a new perspective. Moreover, it allows for controlling the angle stepping accuracy by manipulating variables. Compared with the antennas, the RASs detect the electric field amplitude rather than the electromagnetic power. Therefore, the directionality D for EFES should be expressed as

$$D=\frac{4\pi\|\boldsymbol{E}\|_{\max}}{\int_0^{2\pi}\mathrm{d}\varphi\int_0^{\pi}\|\boldsymbol{E}(\theta,\varphi)\|\sin\theta\mathrm{d}\theta}. \quad (15)$$

Eq. (15) could be used to evaluate the directionality of EFES.

3 Pattern analysis based on CM theory

3.1 Raw model structures for pattern analysis

The proposed current distribution model in Fig. 3 still requires verification to determine its consistency with reality. To quickly verify this theory, the metal material is set as a PEC, and the dielectric material is set as an ideal dielectric with a dielectric constant of 4.2. The resonant frequencies of the four models are the same. Fig. 4 shows the CM analysis for the four models as shown in Fig. 3. The excitation source is a uniform plane wave with unit amplitude,

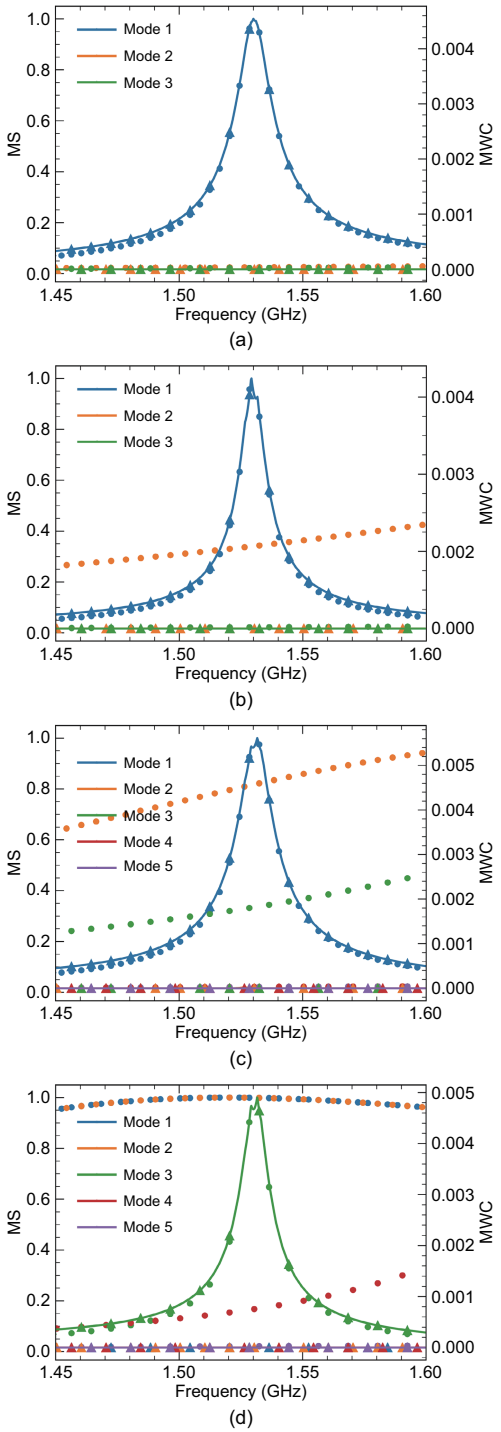

Fig. 4 MS and MWC for four models: (a) path 1; (b) path 2; (c) path 3; (d) path 4. MS data are shown in circle marker, and MWC data are shown in triangle marker

incident along the $-\boldsymbol{e}_x$ direction ($\theta = 90°, \varphi = 0°$). The MS results show that the number of the modes satisfying MS $>$ 0.707 increases with the increase of the current path number. However, the MWC results show that only one mode is excited by the plane wave for each model, concluding that the analyzed models operate in a single mode. Fig. 5 shows the modal current distribution with the highest MWC value for each model, and the corresponding pattern is calculated using Eq. (14). The modal current distribution is consistent with that in Fig. 3. Fig. 6 shows FW simulated patterns for four models. The patterns of four models are analyzed using Eq. (14) and compared with the FW simulation results. The results calculated by the CM method and the FW simulation results are similar, indicating that the CM method can be used to analyze the E-Gain pattern of EFES. Wu et al. (2024) presented an EFES with a current distribution similar to that in path 1, where the patterns are also similar.

3.2 Improved structure for pattern analysis

Wu et al. (2024) specifically verified the model with only one current path. In this study, we verify the accuracy of the proposed method in models with 2, 3, and 4 current paths. The initial design of the structure does not consider the RAS structure that needs to be loaded. Thus, improvements are made to the structures named IP 2, 3, and 4, as shown in Fig. 7. The blue material represents the RAS and the yellow material represents copper.

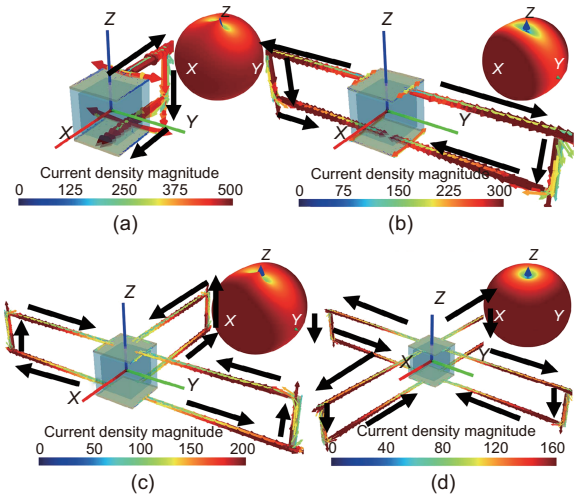

Fig. 5 The modal current and corresponding 3D-view pattern calculated by the CM method at 1.53 GHz: (a) path 1; (b) path 2; (c) path 3; (d) path 4

Fig. 8 shows the CM analysis for the proposed models. To further reveal the coupling degree between the patterns and the plane wave source, we select the largest mode of MWC, which is the mode most excited by the plane wave source. Fig. 8 shows the largest MWC modal currents and the corresponding patterns for each model, calculated using Eq. (14). The modal currents show that the direction of currents is consistent with the proposed theory in Fig. 3.

To verify the results of CM, we simulate the proposed models in CST software. Fig. 9 shows the copolar and crosspolar reception patterns of each model. The results of the FW simulation are obtained by scanning the incident angle of the plane wave source around the spherical surface. The

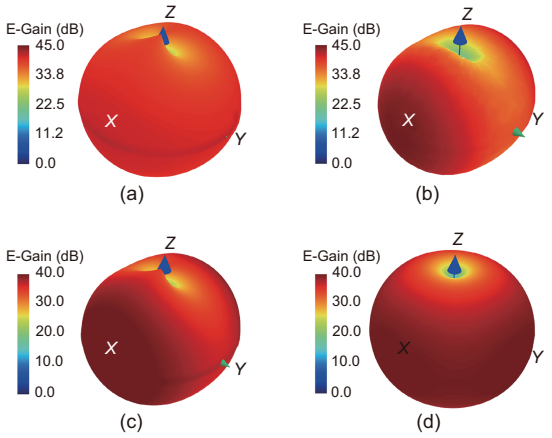

Fig. 6 The 3D-view pattern obtained using FW simulation: (a) path 1; (b) path 2; (c) path 3; (d) path 4

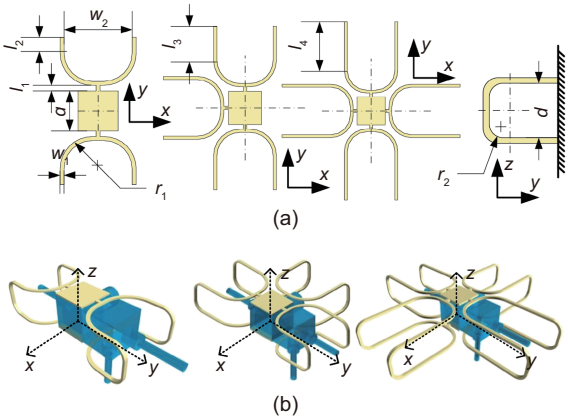

Fig. 7 The configuration of the proposed three models: (a) structure of the models; (b) 3D views of the models. The metal thickness is 0.5 mm. l_1=1 mm, l_2=7 mm, l_3=13.3 mm, l_4=20.4 mm, w_1=1 mm, w_2=17 mm, r_1=7 mm, r_2=3 mm, d=10 mm. References to color refer to the online version of this figure

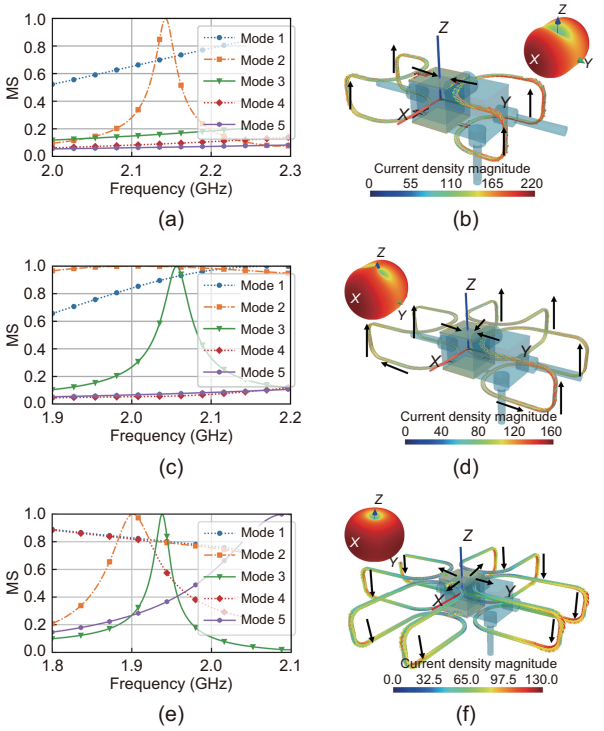

Fig. 8 MS and MWC for four models: (a) MS for IP 2; (b) mode 2 current and patterns of IP 2 at 2.15 GHz; (c) MS for IP 3; (d) mode 3 current and patterns of IP 3 at 2.08 GHz; (e) MS for IP 4; (f) mode 3 current and patterns of IP 4 at 1.96 GHz. Note that the modal current and pattern are obtained when MWC is at its maximum for (b), (d), and (f)

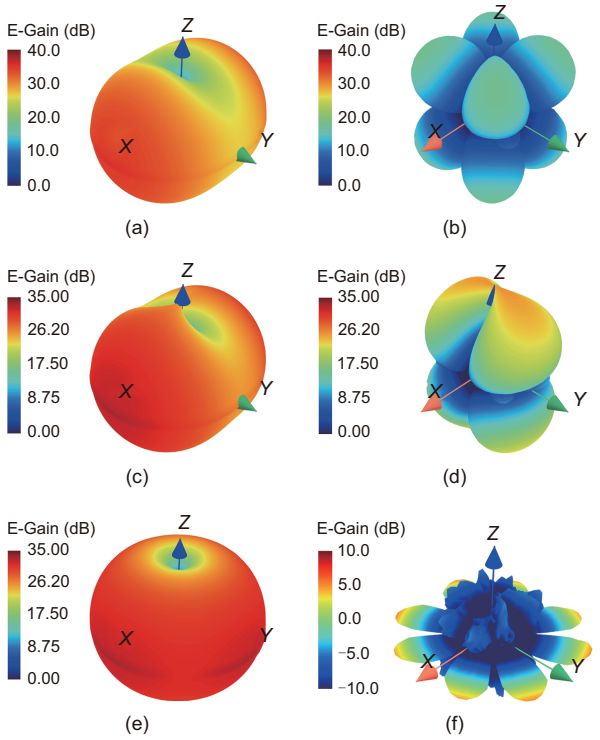

Fig. 9 The 3D-view reception pattern of each model obtained using FW simulation: (a) copolar pattern of IP 2 at 2.15 GHz; (b) crosspolar pattern of IP 2 at 2.15 GHz; (c) copolar pattern of IP 3 at 2.08 GHz; (d) crosspolar pattern of IP 3 at 2.08 GHz; (e) copolar pattern of IP 4 at 1.96 GHz; (f) crosspolar pattern of IP 4 at 1.96 GHz

scanning angles $\Delta\varphi$ and $\Delta\theta$ are 5°, and then they are interpolated to 1° using an interpolation algorithm. It can be observed that the omnidirectionality of the pattern increases with the addition of the path. Table 1 shows the directionality of the IP series calculated by Eq. (14). The omnidirectional performance increases with the increase in the path number. This is because the path represents the modal current, and more paths lead to a more uniform spatial distribution of current, resulting in a more uniform electric field response in the atomic cell center of RAS.

Table 1 Comparison of the directionality of the IP series models

Model	Directionality (dB)	
	FW simulation	CM method
IP 2	2.94	2.46
IP 3	2.47	1.73
IP 4	1.63	1.12
Probe	1.96	NA

NA: not available

It is evident that the patterns calculated based on the CM theory are similar to the shape of the simulated FW. This is a good indication that the proposed method based on the CM theory can guide the pattern design of EFES. Furthermore, using this method requires only a single calculation for CMs to obtain the pattern, reducing the optimization time for pattern design.

4 Measurements and discussion

To validate the proposed design method and operating mechanism, the three models are fabricated and measured. Fig. 10 shows the fabricated prototypes and measurement scenes. First, it is necessary to explain the steps of measuring the experiment results. The first thing to note is the frequency response curve of the E-Gain. The measurement steps are similar to those outlined by Yang et al. (2023c). The details are as follows: (1) connect the experimental instruments with EFES as shown in

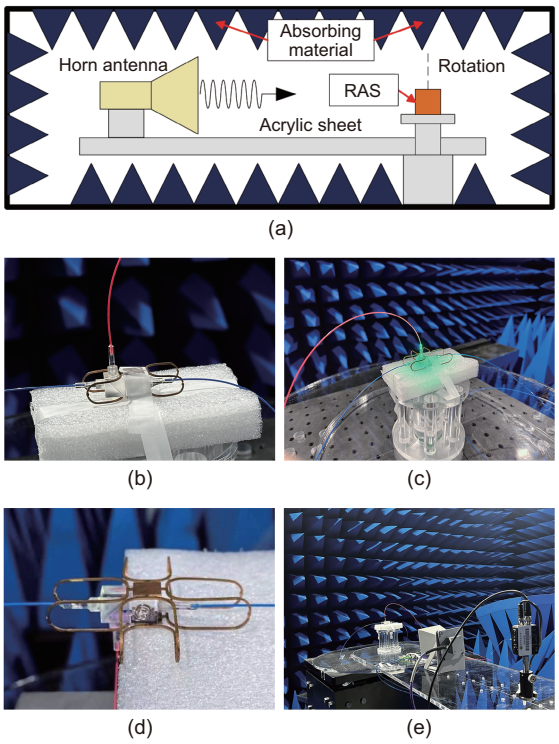

Fig. 10 Diagram and photographs of the fabricated prototypes and measurement scenes: (a) atom reception pattern measurement system diagram; (b) photograph of IP 2; (c) photograph of IP 3; (d) measurement scene of IP 4; (e) measurement scene of IPs 2–4

Fig. 1c; (2) open the RF resource and set a high-level microwave power such as 10 dBm, and define the scanning frequency range and step; (3) traverse each frequency point while recording the shift Δf, and then plot a line showing the relationship between Δf and the source power named curve 1; (4) remove the EFES structure, set the RF source frequency to the peak frequency of curve 1, and then adjust the RF power to match the spacing with the peak shift $\Delta f_{\max}$; (5) traverse each frequency point again to plot a relationship line named curve 2, as in step 3. The power difference between curves 1 and 2 at the same frequency shift Δf_0 is the E-Gain. The frequency response curves can be obtained based on the relative relationship between the variables.

Fig. 11 shows the frequency response curves for the three proposed models. It can be seen that the maximum E-Gain of the measurement results is lower than that of the simulation results. However, the 3-dB-bandwidth of the measurement results is larger than that of the simulation results. It indicates that the measured Q-values are smaller than the simulated ones and that the measured loss is higher. The

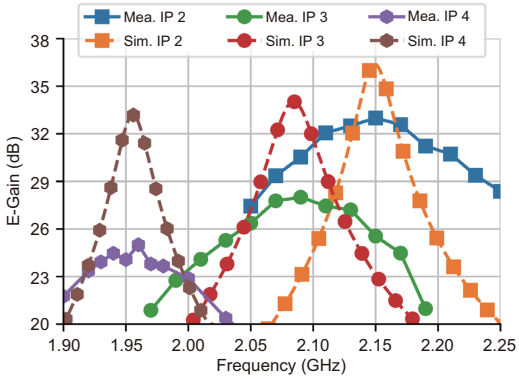

Fig. 11 The simulated and measured frequency response curves for three models

error originates from the losses caused by machining metal materials, which are greater compared to the simulation.

Next, note the measurement steps for the E-Gain pattern measurement setup. The measurement steps are similar to those outlined by Wu et al. (2024) and Yuan et al. (2024). The construction of the antenna pattern measurement system is shown in Fig. 10a. The measurement step details are as follows: (1) connect the experimental instruments with EFES as shown in Fig. 10a; (2) set the RF source frequency to the corresponding structure resonant frequency, and set a high-level microwave power, such as 10 dBm; (3) record the AC-Stark shift Δf as shown in Fig. 1b; (4) rotate the antenna angle, and repeat steps 1 and 2 until a circle is completed.

Fig. 12 illustrates the normalized E-Gain patterns. It is evident that the omnidirectional performance of the proposed models is improved with an increasing number of paths. The variation trends of the measurement results are consistent with those of the simulation results for all models. Table 2 shows some papers similar to this work. This paper demonstrates a commendable ability to balance the E-Gain and out-of-roundness, resulting in the achieved control over the pattern.

To verify whether the method is applicable to higher frequencies, we proportionally reduce the size of structure IP 4 to half of its original dimensions, and compare the results of the CM method with those of the FW method. As shown in Fig. 13, when the resonant frequency of the changed structure is 4.032 GHz, the results from the CM method and the FW method match well, indicating that the method is suitable for higher frequencies.

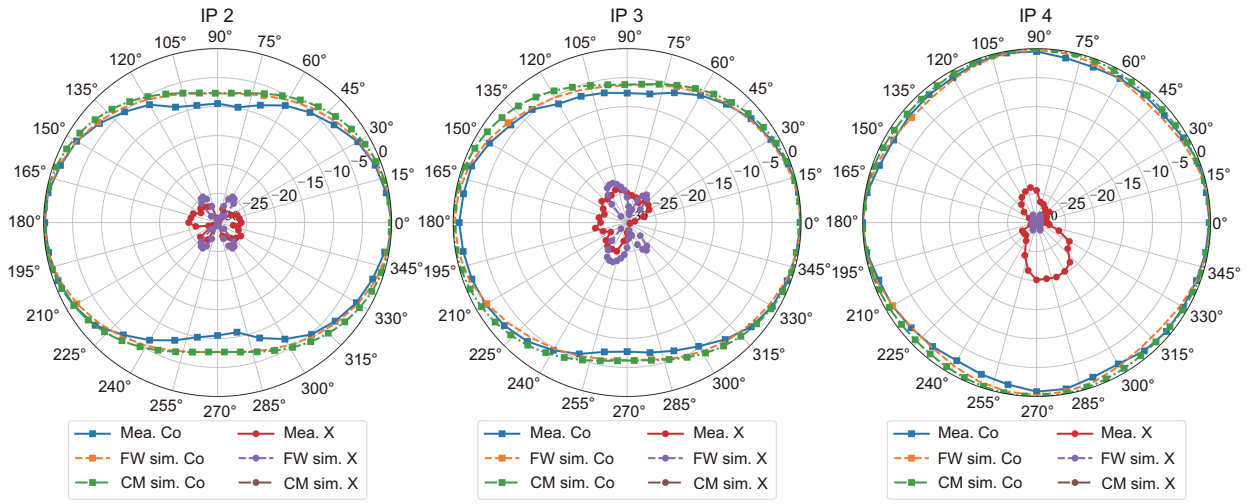

Fig. 12 The simulated and measured normalized reception patterns for the three proposed prototypes ($\theta = 90°$). X refers to cross-polarization, and Co is main polarization

Table 2 Performance comparison

Reference	Frequency (GHz)	Out-of-roundness	E-Gain (dB)
Mao et al. (2023)	4.48	3.50	0
Yuan et al. (2024)	129.60, 4.80	0.28, 2.50	NA
Wu et al. (2024)	2.06	7.80	21.50
This paper			
IP 2	2.15	10.70	33.00
IP 3	2.08	8.80	27.00
IP 4	1.96	2.40	25.00

NA: not available

Combining Eq. (4), the directivity of the structure is related to the incident wave source and the modal current. To simplify the model, we discuss only the situation where the structure is symmetric about the y-axis. At this time, the incident wave along the positive direction of the x-axis and the wave along the negative direction of the x-axis satisfy

$$\boldsymbol{E}^{+}_{\mathrm{inc}}(x) = -\boldsymbol{E}^{-}_{\mathrm{inc}}(-x). \tag{16}$$

According to the analysis in Sections 2.3 and 2.4, the model improved based on symmetry usually operates in a single mode, and it has an even symmetry in current, with the current satisfying

$$\boldsymbol{J}_m(x) = -\boldsymbol{J}_m(-x). \tag{17}$$

Therefore, by combining Eqs. (4), (16), and (17), we can obtain

$$\begin{aligned}\boldsymbol{E} &= \sum_m \frac{<\boldsymbol{E}^{+}_{\mathrm{inc}}(x), \boldsymbol{J}_m(x)>}{1+\mathrm{j}\lambda_m}\boldsymbol{E}_m(\boldsymbol{r}_i)\\ &= \sum_m \frac{<-\boldsymbol{E}^{-}_{\mathrm{inc}}(-x), \boldsymbol{J}_m(x)>}{1+\mathrm{j}\lambda_m}\boldsymbol{E}_m(\boldsymbol{r}_i)\\ &= \sum_m \frac{<-\boldsymbol{E}^{-}_{\mathrm{inc}}(-x), -\boldsymbol{J}_m(-x)>}{1+\mathrm{j}\lambda_m}\boldsymbol{E}_m(\boldsymbol{r}_i)\\ &= \sum_m \frac{<\boldsymbol{E}^{-}_{\mathrm{inc}}(-x), \boldsymbol{J}_m(-x)>}{1+\mathrm{j}\lambda_m}\boldsymbol{E}_m(\boldsymbol{r}_i).\end{aligned} \tag{18}$$

From Eq. (7), it is evident that the responses in the two cases are the same. This indicates that by regulating the symmetry of the current, the response of EFES can be changed, thereby achieving

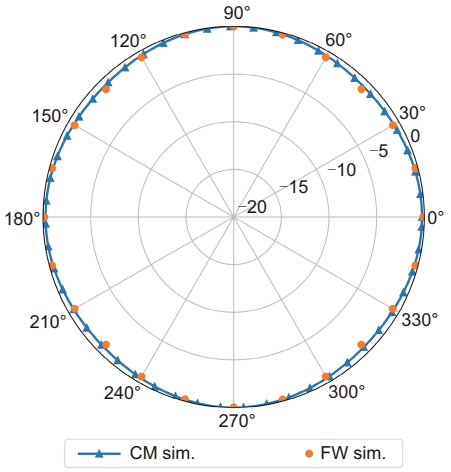

Fig. 13 The pattern of the changed structure for verification at a higher frequency of 4.032 GHz

omnidirectional control of EFES. When the current mode is asymmetric, the results from forward incidence and backward incidence lead to the same response, thus causing asymmetry in the pattern.

5 Conclusions

This paper proposes a pattern analysis method for RAS to design omnidirectional EFES based on the CM theory. We derive new mathematical formulae for pattern analysis of EFES, which can be divided into modal currents and external sources. Modal currents are independent of external sources, and represent an intrinsic property. The shape of modal patterns is determined by modal currents. Only the external source contains the pattern parameters related to the incident angle, which determines the weighting coefficient of each modal pattern in the total pattern. The proposed method guides the analysis and design of EFES by separating parameters. According to the demand of the RASs, the EFES current models are proposed. The mechanism of the current models is analyzed through the CM theory. The directionality of EFESs is changed by controlling the current spatial distribution. The number of the current paths increases, and the symmetry of the structure is enhanced for the improvement of the RASs' omnidirectional performance. To validate the effectiveness of the proposed method, three prototypes are fabricated for measurement. The results indicate that IP 4 achieves good omnidirectional performance, and can enhance the detection sensitivity of the system. This indicates that the proposed CM analysis method is a promising technique for EFES reception pattern analysis. This method lays the foundation for future directional pattern design and high E-Gain design.

Contributors

Zhenke DING designed the research, processed the data, and drafted the paper. Yi LIU analyzed the data, revised the paper, and contributed to the funding acquisition. Bo WU, Kai YANG, Ruibing RAN, and Yi LIN helped process and analyze the data. Yunqi FU helped analyze the data and revise the paper. Yi LIU finalized the paper.

Conflict of interest

All the authors declare that they have no conflict of interest.

Data availability

The data that support the findings of this study are available from the corresponding author upon reasonable request.

References

Adams JJ, Genovesi S, Yang BB, et al., 2022. Antenna element design using characteristic mode analysis: insights and research directions. *IEEE Antenn Propag Mag*, 64(2):32-40. https://doi.org/10.1109/MAP.2022.3145718

Anderson DA, Paradis EG, Raithel G, 2018. A vapor-cell atomic sensor for radio-frequency field detection using a polarization-selective field enhancement resonator. *Appl Phys Lett*, 113(7):073501. https://doi.org/10.1063/1.5038550

Anderson DA, Sapiro RE, Raithel G, 2021. A self-calibrated SI-traceable Rydberg atom-based radio frequency electric field probe and measurement instrument. *IEEE Trans Antenn Propag*, 69(9):5931-5941. https://doi.org/10.1109/TAP.2021.3060540

Bussey LW, Winterburn A, Menchetti M, et al., 2021. Rydberg RF receiver operation to track RF signal fading and frequency drift. *J Lightw Technol*, 39(24):7813-7820. https://doi.org/10.1109/JLT.2021.3098348

Cardman R, Gonçalves LF, Sapiro RE, et al., 2020. Atomic 2D electric field imaging of a Yagi–Uda antenna near-field using a portable Rydberg-atom probe and measurement instrument. *Adv Opt Technol*, 9(5):305-312. https://doi.org/10.1515/aot-2020-0029

Chen Y, Wang CF, 2015. Characteristic Modes: Theory and Applications in Antenna Engineering. John Wiley & Sons, Inc., Hoboken, USA. https://doi.org/10.1002/9781119038900

Choi S, Sarabandi K, 2018. A W-shaped antenna with spatial polarization variation for direction finding. *IEEE Antenn Wirel Propag Lett*, 17(12):2429-2433. https://doi.org/10.1109/LAWP.2018.2877451

Dicandia FA, Genovesi S, 2023. Design of a transmission-type polarization-insensitive and angularly stable polarization rotator by using characteristic modes theory. *IEEE Trans Antenn Propag*, 71(2):1602-1612. https://doi.org/10.1109/TAP.2022.3227459

Dixon K, Nickerson K, Booth DW, et al., 2023. Rydberg-atom-based electrometry using a self-heterodyne frequency-comb readout and preparation scheme. *Phys Rev Appl*, 19(3):034078. https://doi.org/10.1103/PhysRevApplied.19.034078

Fan HQ, Kumar S, Sedlacek J, et al., 2015. Atom based RF electric field sensing. *J Phys B Atom Mol Opt Phys*, 48(20):202001. https://doi.org/10.1088/0953-4075/48/20/202001

Grundmann L, Manteuffel D, 2021. Using characteristic modes for determining the incident field in a scattering problem. Proc IEEE Int Symp on Antennas and Propagation and USNC-URSI Radio Science Meeting, p.855-856. https://doi.org/10.1109/APS/URSI47566.2021.9703784

Harrington RF, 2001. Time-Harmonic Electromagnetic Fields. IEEE Press, New York, USA.

Harrington RF, Mautz J, 1971. Theory of characteristic modes for conducting bodies. *IEEE Trans Antenn Propag*, 19(5):622-628. https://doi.org/10.1109/TAP.1971.1139999

Holloway CL, Gordon JA, Schwarzkopf A, et al., 2014. Sub-wavelength imaging and field mapping via electromagnetically induced transparency and Autler–Townes splitting in Rydberg atoms. *Appl Phys Lett*, 104(24):244102. https://doi.org/10.1063/1.4883635

Holloway CL, Simons MT, Gordon JA, et al., 2019. Detecting and receiving phase-modulated signals with a Rydberg atom-based receiver. *IEEE Antenn Wirel Propag Lett*, 18(9):1853-1857. https://doi.org/10.1109/LAWP.2019.2931450

Holloway CL, Prajapati N, Artusio-Glimpse AB, et al., 2022. Rydberg atom-based field sensing enhancement using a split-ring resonator. *Appl Phys Lett*, 120(20):204001. https://doi.org/10.1063/5.0088532

Hu JL, Jiao YC, He YH, et al., 2023. Improvement of response bandwidth and sensitivity of Rydberg receiver using multi-channel excitations. *EPJ Quant Technol*, 10(1):51. https://doi.org/10.1140/epjqt/s40507-023-00209-7

Huang SD, Pan J, Luo YY, 2018. Study on the relationships between eigenmodes, natural modes, and characteristic modes of perfectly electric conducting bodies. *Int J Antenn Propag*, 2018(1):8735635. https://doi.org/10.1155/2018/8735635

Jiao YC, Han XX, Fan JB, et al., 2019. Atom-based receiver for amplitude-modulated baseband signals in high-frequency radio communication. *Appl Phys Expr*, 12(12):126002. https://doi.org/10.7567/1882-0786/ab5463

Liu B, Zhang LH, Liu ZK, et al., 2022. Highly sensitive measurement of a Megahertz RF electric field with a Rydberg-atom sensor. *Phys Rev Appl*, 18(1):014045. https://doi.org/10.1103/PhysRevApplied.18.014045

Manteuffel D, Lin FH, Li T, et al., 2022. Characteristic mode-inspired advanced multiple antennas: intuitive insight into element-, interelement-, and array levels of compact large arrays and metantennas. *IEEE Antenn Propag Mag*, 64(2):49-57. https://doi.org/10.1109/MAP.2022.3145714

Mao RQ, Lin Y, Yang K, et al., 2023. A high-efficiency fiber-coupled Rydberg-atom integrated probe and its imaging applications. *IEEE Antenn Wirel Propag Lett*, 22(2):352-356. https://doi.org/10.1109/LAWP.2022.3212057

Meyer DH, Cox KC, Fatemi FK, et al., 2018. Digital communication with Rydberg atoms and amplitude-modulated microwave fields. *Appl Phys Lett*, 112(21):211108. https://doi.org/10.1063/1.5028357

Ren K, 2022. Direction finding using a single antenna with blade modulation. *Antenn Wirel Propag Lett*, 21(5):873-877. https://doi.org/10.1109/LAWP.2022.3149871

Robinson AK, Prajapati N, Senic D, et al., 2021. Determining the angle-of-arrival of a radio-frequency source with a Rydberg atom-based sensor. *Appl Phys Lett*, 118(11):114001. https://doi.org/10.1063/5.0045601

Sandidge G, Santamaria-Botello G, Bottomley E, et al., 2024. Resonant structures for sensitivity enhancement of Rydberg-atom microwave receivers. *IEEE Trans Microw Theory Techn*, 72(4):2057-2066. https://doi.org/10.1109/TMTT.2024.3355763

Sedlacek JA, Schwettmann A, Kübler H, et al., 2012. Microwave electrometry with Rydberg atoms in a vapour cell using bright atomic resonances. *Nat Phys*, 8(11):819-824. https://doi.org/10.1038/nphys2423

Sedlacek JA, Schwettmann A, Kübler H, et al., 2013. Atom-based vector microwave electrometry using Rubidium Rydberg atoms in a vapor cell. *Phys Rev Lett*, 111(6):063001. https://doi.org/10.1103/PhysRevLett.111.063001

Shi G, Jia Y, Liu Y, et al., 2023. Theoretic study of antenna scattering problems based on characteristic modes and its applications in reducing antenna scattering. *IEEE Trans Antenn Propag*, 71(3):2098-2109. https://doi.org/10.1109/TAP.2022.3229174

Simons MT, Artusio-Glimpse AB, Holloway CL, et al., 2021. Continuous radio-frequency electric-field detection through adjacent Rydberg resonance tuning. *Phys Rev A*, 104(3):032824. https://doi.org/10.1103/PhysRevA.104.032824

Song ZF, Liu HP, Liu XC, et al., 2019. Rydberg-atom-based digital communication using a continuously tunable radio-frequency carrier. *Opt Expr*, 27(6):8848-8857. https://doi.org/10.1364/OE.27.008848

Wu B, Lin Y, Liao DW, et al., 2022. Design of locally enhanced electric field in dielectric loaded rectangular resonator for quantum microwave measurements. *Electron Lett*, 58(24):914-916. https://doi.org/10.1049/ell2.12618

Wu B, Lin Y, Wu FC, et al., 2023. Quantum microwave electric field measurement technology based on enhancement electric filed resonator. *Acta Phys Sin*, 72(3):034204 (in Chinese). https://doi.org/10.7498/aps.72.20221582

Wu B, Zhou YL, Ding ZK, et al., 2024. Eliminating sensing blind spots of field-enhanced Rydberg atomic antenna via an asymmetric parallel-plate resonator. *EPJ Quant Technol*, 11(1):30. https://doi.org/10.1140/epjqt/s40507-024-00239-9

Yang K, Sun ZS, Mao RQ, et al., 2022. Wideband Rydberg atom-based receiver for amplitude modulation radio frequency communication. *Chin Opt Lett*, 20(8):081203. https://doi.org/10.3788/COL202220.081203

Yang K, Mao RQ, An Q, et al., 2023a. Amplitude-modulated RF field Rydberg atomic sensor based on homodyne technique. *Sens Actuat A Phys*, 351:114167. https://doi.org/10.1016/j.sna.2023.114167

Yang K, Mao RQ, An Q, et al., 2023b. Laser frequency locking method for Rydberg atomic sensing. *Chin Opt Lett*, 21(2):021407. https://doi.org/10.3788/COL202321.021407

Yang K, Mao RQ, He L, et al., 2023c. Local oscillator port embedded field enhancement resonator for Rydberg atomic heterodyne technique. *EPJ Quant Technol*, 10(1):23. https://doi.org/10.1140/epjqt/s40507-023-00179-w

Yao JW, An Q, Zhou YL, et al., 2022. Sensitivity enhancement of far-detuned RF field sensing based on Rydberg atoms dressed by a near-resonant RF field. *Opt Lett*, 47(20):5256-5259. https://doi.org/10.1364/OL.465048

Yuan SX, Jing MY, Zhang H, et al., 2024. Isotropic antenna based on Rydberg atoms. *Opt Expr*, 32(5):8379-8388. https://doi.org/10.1364/OE.517149

Zhang D, Chen YK, Yang SW, 2022. A self-decoupling method for antenna arrays using high-order characteristic modes. *IEEE Trans Antenn Propag*, 70(4):2760-2769. https://doi.org/10.1109/TAP.2021.3125388

Zhang FS, Jin BH, Lan ZT, et al., 2023. Quantum wireless sensing: principle, design and implementation. Proc 29th Annual Int Conf on Mobile Computing and Networking, Article 44. https://doi.org/10.1145/3570361.3613258